Interfacial adhesion of ZnO nanowires on a Si substrate in air – electronic supplementary information

James L. Mead[1], Shiliang Wang[1, 2] *, Sören Zimmermann[3], Han Huang[1] *

S1. Wedge fabrication, transfer, fastening, and substrate inspection procedure

During the formation of a nanowire (NW) arch, contact between the NW and the wedge should occur at a single point to permit simple modelling of the NW's deflected state. Ideal wedge dimensions are determined by considered the geometry of the NW population being tested, which, as presented in Table S4 (ESI S7), have lengths and second moment of areas ranging from $44 - 89 \, \mu m$ and $286.9 - 1.64 \times 10^{-29} \, m^4$, respectively. The height of the wedge dictates how much the NWs deflect, and for this NW population, should remain within the 1-3 µm range. A NW arch with a maximum deflection below 1 µm would exhibit an insufficient number of fringes. A NW arch with a maximum deflection above 3 µm would exhibit fringes that cannot be entirely observed within the focal range of utilised objective lens of the optical microscope (OM) (see 'Experimental details' in the main manuscript), and hence would require micrographs to be taken at different focal heights. The NW arches would also have a large suspended length, requiring NW samples that are long enough to ensure that both ends remain adhered to the substrate. The slope of deflection of small diameter NWs may also become so large that the small-angle approximation being used in the Euler-Bernoulli beam models becomes invalid [1].

Wedge fabrication, transfer, and fastening were carried out by combining focused ion beam (FIB) milling, *in situ* SEM nanomanipulation, and electron beam induced deposition (EBiD) of Pt inside a Scios DualBeam FIB facility (FEI, USA) as per the schematic provided in Fig. S1. Scanning electron microscope (SEM) images of the fabricated wedge are provided in Fig. S2. Commercial carbon fibre segments with a diameter of 7 µm were deposited onto the surface of a 'preparatory' Si substrate, as shown in Fig. S2a. The carbon fibre was then FIB milled into a symmetric wedge shape using a $0.5 - 15 \, nA$ and 20 kV ion beam current range and acceleration voltage, respectively (Fig. S1a-c). It was crucial that the region of the substrate surface for which adhesion testing was conducted was not modified by the FIB. The milled carbon fibre was therefore Pt fastened to a W probe and transferred to a 'pristine' Si substrate (Fig. S1d and e). FIB milling was used to cut-free the modified carbon fibre from the W probe. It was ensured that the FIB's field of view remained outside of the region of the substrate reserved for NW arch placement and testing (Fig. S1f). The FIB damaged region of the surface was therefore restricted to only one end of the modified carbon fibre (Fig. S1g). The modified carbon fibre was then fastened at each end to the substrate using Pt deposition to ensure the wedge structure was unmoveable during the formation and removal of NW arches (Fig. S1h). A top down view of the final fastened wedge structure is shown in Fig. S2b.

After removal from the SEM the substrate was heated to 400°C in atmosphere in order to vaporise EBiD carbon from its surface. The condition of the substrate surface within the vicinity of the wedge was then investigated using optical microscopy, as shown in Fig. S2c. Substrate regions are demarcated from i to iv. The FIB damaged region (i) is clearly distinguishable from the pristine test region (ii). Pt residue immediately surrounding each end of the wedge (iii), and the FIB-milled trench (iv) is also evident. These observations were used as a reference to ensure that all NW arches were formed entirely within the pristine test region.
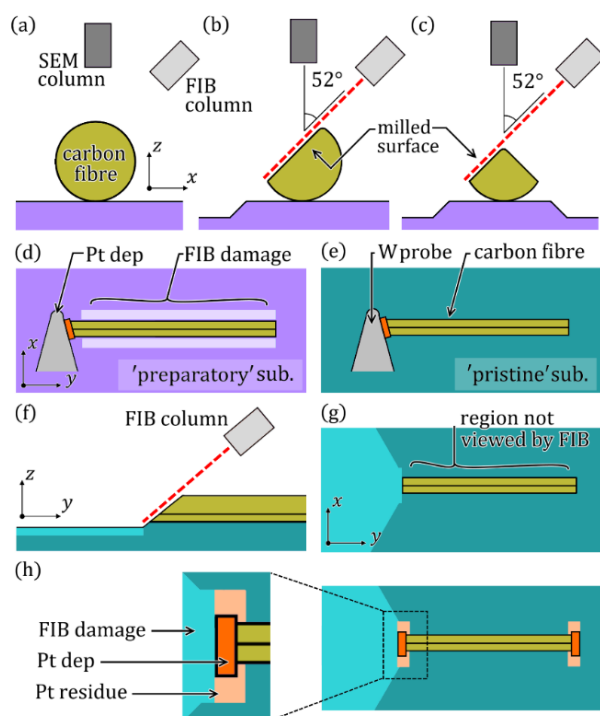

Fig. S1 *Fabrication procedure of the wedge structure. (a) Deposition of a carbon fibre onto a 'preparatory' substrate, followed by FIB-milling of the (b) left and (c) right sides to form a symmetric triangular-shaped wedge. (d) EBiD of Pt was used to fasten the carbon fibre to the W probe; facilitating its transfer from the preparatory substrate to a (e) 'pristine' substrate. (f) FIB-cutting of the carbon fibre to detach it from the W probe, (g) ensuring that FIB-damage was restricted to a region adjacent to the carbon fibre. (h) Fastening of the carbon fibre to the substrate using Pt deposition.*
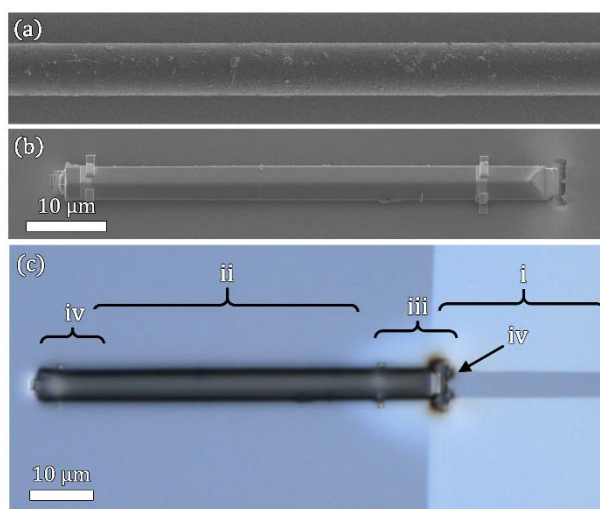

Fig. S2 *(a) Unmodified carbon fibre. (b) FIB-milled wedge structure. (c) Optical micrograph of the area of the substrate surrounding the wedge. Substrate regions are demarcated i-iv. (i) FIB-damaged region, (ii) pristine test region, (iii) platinum residue, (iv) FIB-milled trench.*

S2. Non-ideal geometry of a nanowire

A NW with a regular hexagonal cross-section (see Fig. 3a in the main manuscript) has six facets with equal facet-length, a_{avg}, which can be defined in terms of t or w by the following geometric relations; $a_{avg} = (\sqrt{3}/3)t = w/2$. A NW with an irregular hexagonal cross-section is assumed to be symmetric about its y and z axis, and to maintain 120° internal angles (see Fig. 3b in the main manuscript). The top and bottom facet therefore have a different length to the four side facets. The top/bottom facets have an equal major facet-length, a_1, and the side facets have an equal minor facet-length, a_2. Derivation of the major and minor facet lengths require both t and w by the following geometric relations; $a_1 = w - (\sqrt{3}/3)t$, and $a_2 = (\sqrt{3}/3)t$, respectively. The second moment of area of a NW with a regular and irregular cross-section, I_{reg} and I_{irr}, can then be defined as per eqn (S3) and (S4) (Table S1), respectively.

It is useful to examine the properties of NWs as a function of a size parameter, especially as NWs are commonly found to exhibit size-effects. [2-4] This requires the definition of a NW's size. As 'size' is an arbitrary property, it is important to select a definition that relates to a physical property associated with size-effects. Size-effects observed in NWs have commonly been associated with a relative increase in the NW's surface area, where surface stiffening [2,3] and surface defects [4] can occur. In this study, we express the size of a NW with a regular hexagonal cross-section by an effective diameter parameter, $D_{e,reg}$, equivalent to two times its facet-length. We also define an effective diameter for an irregular hexagonal NW, $D_{e,irr}$, by specifying that it must have an equivalent volume to surface ratio per unit length to a regular hexagonal NW of the same effective diameter. To derive this expression, we first determine the volume, V_{reg} and V_{irr}, and surface area, SA_{reg} and SA_{irr}, of NWs with regular and irregular hexagonal cross-sections, in terms of their facet-lengths, a_{avg}, a_1, a_2, as well as their length, L, as per eqn (S5), (S6), (S7), and (S8) (Table S1), respectively. Note that the end surfaces of a NW are not considered. The volume-to-surface ratios for regular and irregular NWs, $(V/SA)_{reg}$ and $(V/SA)_{irr}$, can then be defined as per eqn (S9) and (S10) (Table S1), respectively. This allows $D_{e,irr}$ to be expressed in terms of the major and minor facet-lengths as per eqn (8) in the main manuscript.

The irregularity of a NW's cross-section can be expressed using an irregularity ratio, $Z = a_1/a_2$, where, for simplicity, we considered it to remain constant over the axial length of a NW. Additionally, the degree to which a NW is tapered is determined by evaluating the geometry of its cross-section at each of its ends, as per the schematic in Fig. S3a. Note, we consider that tapering occurs linearly over its length. The non-ideal geometry of a tapered and irregular NW can therefore by fully defined by considering just three dimensional parameters; irregularity ratio, degree of tapering, and major facet-length, a_1, calculated at the wedge contact-point. The irregularity ratio of a NW is taken as the average of the facet-length values obtained from both its ends. The degree of tapering can be defined by:

$$\frac{da_1}{dx} = \left(\frac{a_{1,right} - a_{1,left}}{L_{left} + L_{right}} \right) \tag{S1}$$

where dx is an increment of the NW's length, $a_{1,left}$ and $a_{1,right}$ are the major facet-lengths measured at locations at the left and right ends of the

NW, defined by their distances of L_{left} and L_{right} from the wedge contact-point, respectively. The major facet-length value at the wedge contact-point can then be determined and used as a reference:

$$a_{1,wedge} = a_{1,left} + \left(\frac{da_1}{dx} \right) L_{left} \tag{S2}$$

High-resolution SEM and AFM micrographs obtained at approximately the same location at one end of a typical NW arch (NWA3) are presented in Fig. S3b and c, respectively. The faceted surface of the NW is clearly observable in the SEM micrograph. An AFM line-profile (LP) of the cross-section of the NW is presented in Fig. 3d; located as demarcated by the dotted line in the AFM micrograph. The overlayed hexagon defines the theoretical irregular cross-section of the NW, deduced from the t and w measurements. The geometric parameters for all 11 tested NWs are listed in Table S4 (ESI S7). Note, parameter values determined at the wedge contact-point are notated with the subscript 'wedge'. The irregularity ratio and degree of tapering for all tested NWs are plotted with respect to their equivalent effective diameter in Fig. S4a and b, respectively.
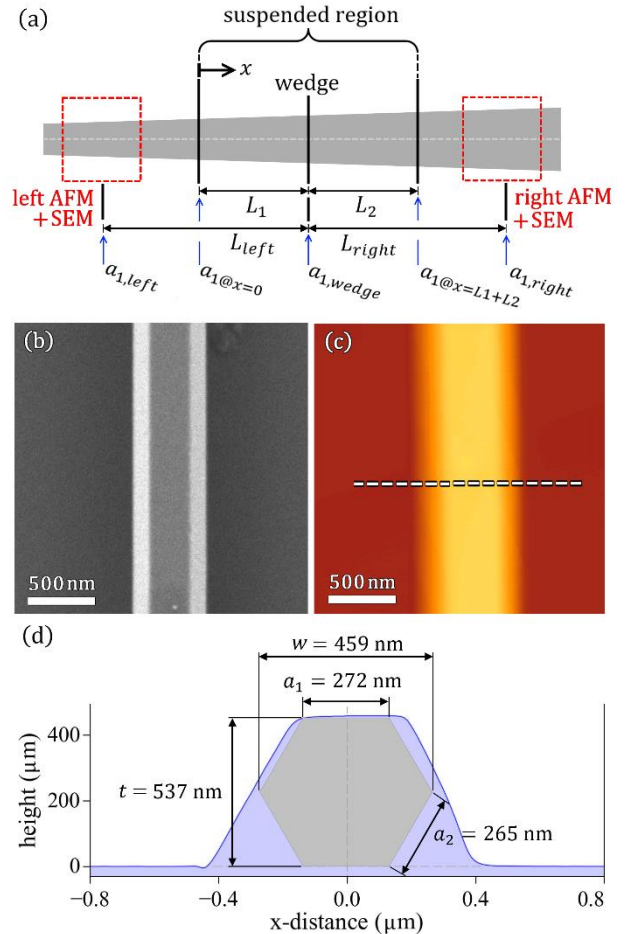
Fig. S3 (a) Schematic of the tapered geometry of a NW, showing the locations of AFM and SEM examination, and how their distances from the wedge contact-point are defined. (b) SEM, and (c) AFM micrographs showing the faceted surface of a typical NW (NWA3), used for measuring its thickness and width, respectively. (d) AFM line-profile of the NW's cross-section, located as demarcated by the dotted line in the AFM micrograph. The overlayed hexagon provides the theoretical cross-section of the NW, deduced from the width and height measurements.

Table S1. *Equations for the second moment of area, volume, surface area, and volume-to-surface ratio of NWs with regular and irregular hexagonal cross-sections.*

	Regular cross-section		Irregular cross-section	
Second moment of area (m^4)	$I_{reg} = \dfrac{5\sqrt{3}}{16} a_{avg}^{\;4}$	(S3)	$I_{irr} = \dfrac{\sqrt{3}}{16} a_1^{\;3}\left(4a_1 + a_2\right)$	(S4)
volume, V (m^3)	$V_{reg} = (3\sqrt{3}/2)a_{avg}^{\;2}L$	(S5)	$V_{irr} = (\sqrt{3}/2)(2a_1 + a_2)a_2 L$	(S6)
surface area, SA (m^2)	$SA_{reg} = 6a_{avg}L$	(S7)	$SA_{irr} = 3(a_1 + a_2)L$	(S8)
volume-to-surface ratio, V/SA (m)	$\left(\dfrac{V}{SA}\right)_{reg} = \dfrac{\sqrt{3}}{4} a_{avg}$	(S9)	$\left(\dfrac{V}{SA}\right)_{irr} = \dfrac{a_2\left(2a_1 + a_2\right)}{2\sqrt{3}\left(a_1 + a_2\right)}$	(S10)
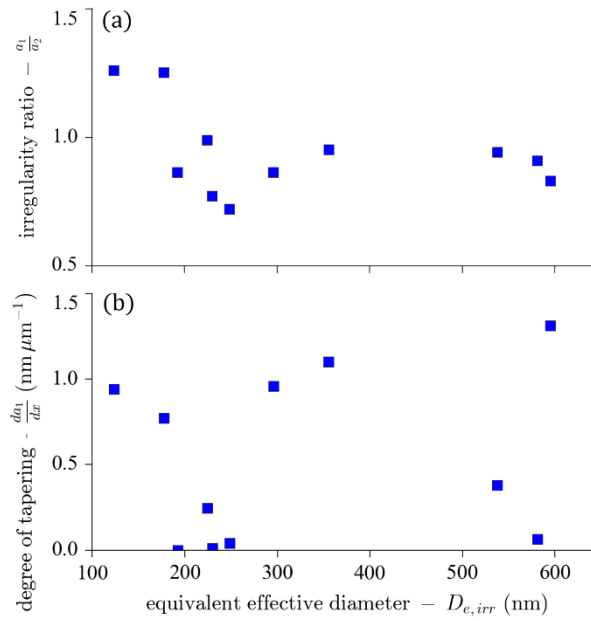
Fig. S4 (a) Irregularity ratio of the cross-section, and (b) degree of tapering for all tested NWs, plotted with respect to their equivalent effective diameter.

S3. Nanowire arch deflection formulae

'Half-arch' model

The generalised internal moment distribution of a clamped-clamped unloaded beam as described by the 'half-arch' model, can be determined by considering the free body diagram presented in Fig. 3c of the main manuscript. Considering the left side of a NW arch; at the location of the crack front, designated point A, $x = 0$, $\delta = 0$, $(d\delta/dx) = 0$, and an external moment, M_a, and vertical reaction, $F_{v,a}$, are applied. Note that the origin of x is always taken from point A. At the location where the NW contacts the wedge, designated point B, $x = s$, $\delta = h$, $(d\delta/dx) = 0$, and M_b as well as $F_{v,b}$, are applied. The general solution for the internal moment distribution in the beam can then be defined as $M_i = F_{v,a} - M_a$. Double integration of the moment-curvature relationship [5] using the above stated boundary conditions yields a unique solution for deflection along half of the suspended length of a NW arch, as per eqn (1) in Table 1 of the main manuscript. Parameters, h and s, obtained from fitting the deflection equation to the co-ordinates obtained for the left and right sides of a NW arch (Table S5 and S6) are provided in Table S7 (ESI S7). Coefficients of regression are also provided to assess the goodness of fit.

'Full-arch' model

The generalised internal moment distribution of the clamped-clamped beam with arbitrary point-load, as described by the 'full-arch' model, can be determined by considering the free body diagram presented in Fig. 3d of the main manuscript. Again, at point A, $x = 0$, $\delta = 0$, $(d\delta/dx) = 0$, and M_a as well as $F_{v,a}$, are applied. Considering the right side of the NW arch; at the location of the crack front, designated point C, $x = L_1 + L_2$, $\delta_1 = 0$, $(d\delta_1/dx) = 0$, and M_b as well as $F_{v,b}$, are applied. At the location where the NW contacts the wedge, designated point B, $x = L_1$, $\delta_1 = \delta_2 = h_w$, $(d\delta_1/dx) = (d\delta_2/dx)$, and P is applied. The general solution for the internal moment distribution in the left segment of the beam is the same as for the half-arch model, and the right segment is defined by $M_{i2} = \left(F_{v,a} - M\right)x - PL_1 - M_a$. The unique solution for deflection along the suspended length of a NW arch can then be determined for both the left and right sides; see eqn (3) and (4) in Table 1 of the main manuscript.

For a tapered NW, the major facet-length can be expressed as a function of x:

$$a_1(x) = a_{1,wedge} + \frac{da_1}{dx}(x - x_{wedge}) \tag{S11}$$

where $a_{1,wedge}$ is the major facet-length at the wedge contact-point, da_1/dx is the degree of tapering (see eqn (S2) and (S1)), and x_{wedge} is the x co-ordinate of the wedge contact-point where point A is the reference. A tapered NW's cross-sectional area can then be expressed in terms of the major facet-length function. Note that a_2 tapers proportionally to a_1, and so can be alternatively expressed using the irregularity ratio, giving:

$$I_{irr,taper}(x) = \frac{\sqrt{3}}{16}\left[a_1(x)\right]^4\left(4 + Z^{-1}\right) \tag{S12}$$

Substituting eqn (S11) into eqn (S12) allows the NW's second moment of area to be expressed as a function of x:

$$I_{irr,taper}(x) = \frac{\sqrt{3}}{16}\left(4 + Z^{-1}\right)\left(a_{1,wedge} + \frac{da_1}{dx}\left(x - x_{wedge}\right)\right)^4 \tag{S13}$$

Replacing I_{irr} with $I_{irr,taper}$ in the flexural formula yields updated deflection equations for the full-arch model, defined by eqn (4) and (5) in Table 1 of the main manuscript. Parameters, h_w, L_1, L_2, and x_{wedge} obtained from fitting both the ideal and tapered deflection equations to the co-ordinates obtained for the left and right sides of a NW arch (Table S5 and S6) are provided in Table S8 (ESI S7). Coefficients of regression are also provided to assess the goodness of fit.

S4. Interfacial adhesion formulae

Non-tapered nanowire – 'half-arch' and 'full-arch' models

Internal moment distribution

Employing the half-arch model, the internal moment distribution within a non-tapered NW arch is defined by:

$$\frac{M_{i,H-B}}{EI} = -\frac{12h}{s^3}x + \frac{6h}{s^2} \tag{S14}$$

Employing the full-arch model, the internal moment distributions within the left and right sides of a non-tapered NW arch are defined by:

$$\frac{M_{i1,F-B}}{EI} = -\frac{3h}{L_1^3 L_2}\left((3L_1 + L_2)x - L_1(L_1 + L_2)\right) \tag{S15}$$

$$\frac{M_{i2,F-B}}{EI} = -\frac{3h}{L_1 L_2^3}\left((L_1 + 3L_2)x - (L_1 + L_2)(L_1 + 2L_2)\right) \tag{S16}$$

Elastic strain energy

The elastic strain energy is determined by integrating the internal moment distribution along the detached length of the NW [6]:

$$U_E = \frac{1}{2EI}\int_0^s \left(M_i\right)^2 dx \tag{S17}$$

Employing the half-arch model, the elastic strain energy for a NW arch with an arbitrary cross-section is defined by:

$$U_{E,H-B} = \frac{6h^2 EI}{s^3} \tag{S18}$$

Employing the full-arch model, the elastic strain energy for a NW arch with an arbitrary cross-section is defined by:

$$U_{E,F-B} = \frac{3h^2(L_1 + L_2)^3 EI}{2L_1^3 L_2^3} \tag{S19}$$

Total adhesion energy

The total adhesion energy is determined by considering the interfacial area formed between the NW and substrate:

$$U_{A,H-B} = -\Gamma w L_{ad} \tag{S20}$$

where Γ is the adhesion energy per unit interfacial area, w is the width of the interfacial area (i.e. the bottom facet-length of the NW), and L_{ad} is the total adhered length. Employing the half-arch model, the total adhesion energy for a NW arch with an arbitrary cross-section is defined by:

$$U_{A,H-B} = -\Gamma w(l - s) \tag{S21}$$

Employing the full-arch model, the total adhesion energy for a NW arch with an arbitrary cross-section is defined by:

$$U_{A,F-B} = -\Gamma w\left(l - (L_1 + L_2)\right) \tag{S22}$$

Interfacial adhesion energy per unit area

The total energy of a NW arch, denoted as $U_{T,H-B}$ and $U_{T,F-B}$ when using the half-arch and full-arch model, respectively, is simply quantified by summing the elastic strain energy and the total adhesion energy. When a NW arch is at an equilibrium state, the derivative of its total energy with respect to its detached length is equal to zero. Specifically, for the half-arch model, $dU_{T,H-B}/ds = 0$, and for the full-arch model, $\partial U_{T,F-B}/\partial L_1 + \partial U_{T,F-B}/\partial L_2 = 0$. As the detached length of the NW approaches the critical length, i.e. as $s \to l$ for the half-arch model, and $L_1 + L_2 \to l$ for the full-arch model, the interfacial adhesion energy per unit area can be determined. Employing the half-arch model, the interfacial adhesion energy per unit area for a NW arch with an arbitrary cross-section is given by eqn (6) in the main manuscript. If the NW has a regular cross-section, its energy is given by eqn (9) in the main manuscript. If the NW has an irregular cross-section, its energy is given by:

$$\Gamma_{H-B,irr} = -\frac{9\sqrt{3}h^2 E a_1^2(4a_1 + a_2)}{8s^4} \tag{S23}$$

Employing the full-arch model, the interfacial adhesion energy per unit area for a NW arch with an arbitrary cross-section is given by eqn (7) in the main manuscript. If the NW has a regular cross-section, its energy is given by:

$$\Gamma_{F-B,reg} = -\frac{45\sqrt{3}h^2(L_1 + L_2)^2(L_1^2 + L_2^2)E a_{avg}^3}{64L_1^4 L_2^4} \tag{S24}$$

If the NW has an irregular cross-section, its energy is given by:

$$\Gamma_{F-B,irr} = -\frac{9\sqrt{3}h^2\left(L_1+L_2\right)^2\left(L_1^2+L_2^2\right)Ea_1^2\left(4a_1+a_2\right)}{64L_1^4L_2^4} \tag{S25}$$

Tapered nanowire – full-arch model

Internal moment distribution

The internal moment distribution within the left and right sides of a tapered, irregular NW arch can be defined with respect to the NW's degree of tapering by:

$$M_{i1,F-B,taper} = -\frac{3\sqrt{3}}{16L_1^3L_2}Q_1\left[\left(a_1\left(3L_1+L_2\right)+\frac{da_1}{dx}\left(2L_1\left(L_1+L_2\right)-x_{wedge}\left(3L_1+L_2\right)\right)\right)x - L_1\left(L_1+L_2\right)\left(a_1-\frac{da_1}{dx}x_{wedge}\right)\right]$$

where $Q_1 = hE\left(4+Z\right)\left(a_1-\frac{da_1}{dx}x_{wedge}\right)\left(a_1+\frac{da_1}{dx}\left(L_1-x_{wedge}\right)\right)^2$ $\hspace{2cm}$ (S26)

$$M_{i2,F-B,taper} = \frac{3\sqrt{3}}{16L_1L_2^3}Q_2\left[\left(a_1\left(L_1+3L_2\right)+\frac{da_1}{dx}\left(\left(L_1+L_2\right)^2-x_{wedge}\left(L_1+3L_2\right)\right)\right)x - \left(L_1+L_2\right)\left(a_1\left(L_1+2L_2\right)+\frac{da_1}{dx}\left(L_1^2+L_1L_2-x_{wedge}\left(L_1+2L_2\right)\right)\right)\right]$$

where $Q_2 = hE\left(4+Z\right)\left(a_1+\frac{da_1}{dx}\left(L_1+L_2-x_{wedge}\right)\right)\left(a_1+\frac{da_1}{dx}\left(L_1-x_{wedge}\right)\right)^2$ $\hspace{2cm}$ (S27)

Total adhesion energy

Employing the full-arch model, the total adhesion energy for a NW arch with a tapered cross-section can be defined by considering that the interfacial area is a trapezoid:

$$U_{A,F-B,taper} = \Gamma\left(\frac{a_{1@\,x=0}+a_{1@\,x=L1+L2}}{2}\right)\left(l-L_1+L_2\right) \tag{S28}$$

where $a_{1@\,x=0}$ and $a_{1@\,x=L1+L2}$ are the major side-lengths at the left and right crack fronts, respectively. At equilibrium, they can then be expressed in terms of the reference major facet-length, their distance from the wedge contact-point, and the degree of tapering, respectively:

$$a_{1@\,x=0} = a_{1,wedge} - \frac{da_1}{dx}x_{wedge} \tag{S29}$$

$$a_{1@\,x=L1+L2} = a_{1,wedge} + \frac{da_1}{dx}\left(L_1+L_2-x_{wedge}\right) \tag{S30}$$

The total adhesion energy for a NW arch can now be defined with respect to the degree of tapering:

$$U_{A,F-B,taper} = -\Gamma\left(l-\left(L_1+L_2\right)\right)\left(a_{1,wedge}+\frac{da_1}{dx}\left(\frac{L_1+L_2-2x_{wedge}}{2}\right)\right) \tag{S31}$$

Derivation of the stored elastic strain energy, and subsequently, the interfacial adhesion energy per unit area of a tapered NW arch was undertaken in the same manner as for a non-tapered NW. However, the analytical solutions were impractically long to present here, and were implemented numerically in order to calculate the non-idealised energy values plotted in Fig. 5b in the main manuscript. The interfacial adhesion energy per unit area values obtained for all NWs when using, (1) the half-arch model, and assuming ideal NW geometry, (2) the full-arch model, and assuming ideal NW geometry, and (3), the full-arch model, and accounting for the irregular and tapered cross-section of a NW are provided in Table S9 and S10 (ESI S7).

S5. VdW interaction energies and Hamaker constants for interfacial systems

The native and thermally grown SiO_2 film of the as-received and heat-treated Si substrates, respectively, were measured using a VUV-variable angle spectroscopic ellipsometer (J.A. Woollam Co., Inc. USA). Amplitude and phase difference data was acquired at incidence angles of 65°, 70°, and 75° in the wavelength range of 300-1600 nm. Film thickness was extracted by fitting a Cauchy dispersion model to the data. The as-received and heat-treated Si substrates exhibited oxide layer thicknesses of 2.57 and 2.81 nm, respectively. This shows that the heat-treatment of the substrate prior to testing negligibly increased the oxide thickness. The vdW interaction potential between two atoms inversely scales with their separation distance to the power of six. [7] Therefore, as the oxide layer thickness of the Si substrate is above 2 nm, the vdW interaction at the NW-substrate interface can be primarily associated with the dielectric response of the oxide layer. The vdW interaction between a ZnO NW and both a SiO_2 and Si surface were selected for evaluation in order to establish how recognition of the oxide layer provides a significantly different theoretical adhesion energy. Furthermore, the interface was evaluated at an entirely dry state – when the surfaces are separated by air; and an entirely wet state – when the surfaces are separated by molecules of water. Four theoretical interfacial systems of interest were therefore evaluated; ZnO-water-SiO_2, ZnO-air-SiO_2, ZnO-water-Si, and ZnO-air-Si.
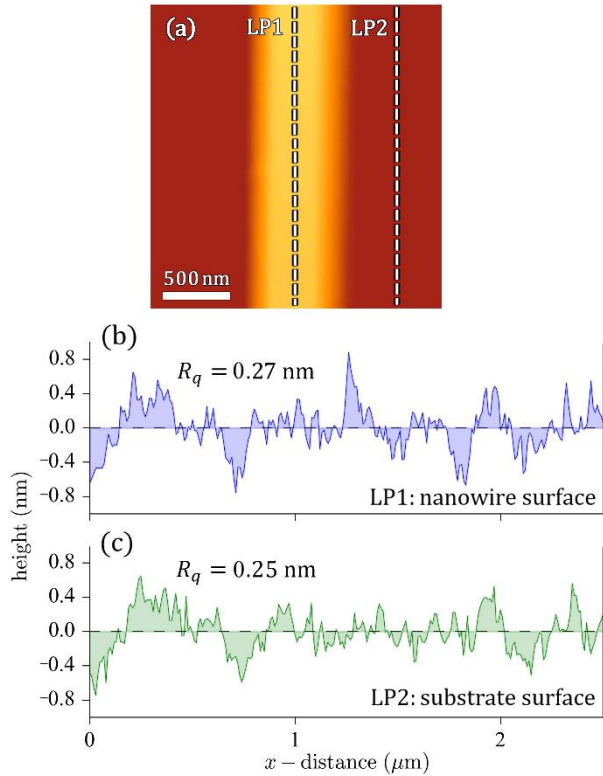

Fig. S5 *(a) AFM micrograph a typical NW (NWA3) deposited on a Si substrate, used for calculated the surface roughness of both the NW and substrate. AFM line-profiles of (b) the surface of a NW, along its longitudinal axis (LP1), and (c) the Si substrate (LP2). The location of the line-profiles are demarcated by the dotted line in the AFM micrograph.*

Surface examination of a typical ZnO NW on the Si substrate was conducted using AFM, and the micrograph is provided in Fig. S5a. LPs of the NW and substrate surface are presented in Fig. S5b and c, respectively, and are aligned parallel to the longitudinal axis of the NW as demarcated by the dotted lines in Fig. S5a. The respective LPs provide $R_q = 0.27$ nm and 0.25 nm for the NW and substrate. The vdW

interaction energy of each interface is quantified by a parallel plate model: [8]

$$\gamma_{vdW} = \frac{A_{132}}{12\pi d_{avg}^{2}} \tag{S32}$$

where A_{132} is the Hamaker constant for the specific interfacial system. The sum of R_q values for each surface is $d_{avg} = 0.52$ nm . [9] Note, that a more accurate determination of R_q was conducted by DelRio *et al.* by lowering the AFM examined topography of one surface onto that of the other until an asperity contact occurred, and then summing the separation computed at every pixel. [10] Such a method accounts for when asperities on one surface fit into the trough of the other, and is expected to predict a smaller separation.

To evaluate the Hamaker constant of the system, pair-wise summation of all atom-atom interactions as introduced by Hamaker [11] is not sufficient for approximating the interaction between two bodies through a medium, and therefore we implemented the continuum approach presented by Dzyaloshinskii-Lifshitz-Pitaevskii. [12] As such, the non-retarded Hamaker constant for two macroscopic half-spaces, 1 and 2, interacting over a medium 3 is given by: [12-14]

$$A_{132} = \frac{3kT}{2} \sum_{m=0}^{\infty}{}' \sum_{s=1}^{\infty} \frac{\left(\Delta_{13}\Delta_{23}\right)}{s^{3}} \tag{S33}$$

where, k is Boltzmann's constant, and T is the absolute temperature of the system, the prime on the summation denotes the zero frequency term is halved, and:

$$\Delta kl = \frac{\varepsilon_k\left(i\xi_m\right) - \varepsilon_l\left(i\xi_m\right)}{\varepsilon_k\left(i\xi_m\right) + \varepsilon_l\left(i\xi_m\right)} \tag{S34}$$

where $\varepsilon_k\left(i\xi_m\right)$ and $\varepsilon_l\left(i\xi_m\right)$ are the dielectric response functions of material k and l, respectively, when evaluated at the imaginary frequencies, $i\xi_m$, where $\xi_m = m \times \left(4\pi^2 kT\right)/h$, where h is Planck's constant. The dielectric response functions can be described using a Lorentz harmonic-oscillator model using the Ninham-Parsegian representation: [15, 16]

$$\varepsilon\left(i\xi\right) = 1 + \sum_{q=1}^{N} \frac{C_q}{1 + \left(\frac{\xi}{\omega_q}\right)^2 + \frac{\gamma_q \xi}{\omega_q^2}} \tag{S35}$$

where C_q, ω_q, and γ_q are the spectral constants (related to the absorption strengths), the characteristic absorption frequencies, and the related damping coefficients of the oscillator in the infrared and ultraviolet range of the materials and media, respectively. Table S2 summarised the C_q, ω_q, and γ_q parameters used to construct $\varepsilon\left(i\xi\right)$ for each interface material and media of interest in this study. Parameters describing absorption frequencies within the infrared and ultraviolet range are denoted with subscripts 'IR' and 'UV', respectively. Three respective absorption peaks are described in order to construct the dielectric response within the UV spectrum for both SiO_2 and Si. Five and six respective absorption peaks are described in order to construct the dielectric response within the UV and IR spectrum for water. The Hamaker constants and vdW interactions energies for each interfacial system of interest, derived from eqn (S32), (S33), (S34), and (S35) are provided in Table S3.

Table S2. *Spectral parameters, C_q , ω_q , and γ_q , used to construct $\varepsilon(\mathrm{i}\xi)$ for each interface material and media.*

	C_{IR}	$\omega_{IR}\times10^{14}$ (rad/s)	$\gamma_{IR}\times10^{13}$ (rad/s)	C_{UV}	$\omega_{UV}\times10^{16}$ (rad/s)	$\gamma_{UV}\times10^{15}$ (rad/s)
ZnO [17]	8.15	0.7	0	2.648	0.895	0
SiO$_2$ [14]	0.829 0.095 0.798	0.867 1.508 2.026	0	1.098	2.034	0
Si [14]	0.043 0.050 0.059	0.345 0.535 0.884	0	10.448	0.503	0
water [14, 18]	1.4635 0.7368 0.1526 0.0136 0.0751	0.314 1.047 1.396 3.065 6.450	2.29 5.78 4.22 3.81 8.54	0.0392 0.0570 0.0923 0.1556 0.1522 0.2711	1.2593 1.5172 1.7296 1.9724 2.2606 2.8068	0.774 1.335 2.336 3.110 4.491 9.498

Table S3. *Hamaker constants and vdW interaction energy for each interfacial system.*

	$A_{132}\times10^{-20}$ (J)	γ_{vdW} (mJ m^{-2})
ZnO-water-SiO$_2$	0.758	0.74
ZnO-air-SiO$_2$	7.377	7.24
ZnO-water-Si	4.589	4.50
ZnO-air-Si	13.025	12.78

S6. Uncertainty analysis

The obtained adhesion energy per unit interfacial area values are associated with multiple sources of experimental uncertainty. Precise determination of a NW's facet-lengths at the wedge contact-point, $a_{avg,wedge}$, $a_{1,wedge}$, and $a_{2,wedge}$ is limited by the spatial resolution of the AFM and SEM used to measure t and w at the ends of a NW, in combination with the optically measured distance between the end of a NW to its wedge contact-point, L_{left} and L_{right} . Absolute uncertainties of $\Delta a_{avg,wedge}=\Delta a_{1,wedge}=\Delta a_{2,wedge}=\pm5$ nm are defined. We also define an absolute uncertainty of $x_{wedge}=\pm1$ μm for the x co-ordinate of the wedge contact-point. The facet-lengths and x co-ordinate of the wedge contact-point are also used to evaluate the degree of tapering of a NW; an absolute uncertainty of $\Delta da_1/dx=0.1$ nm/μm is therefore defined. Precise determination of the deflection equation fitting parameters, s , L_1 , L_2 , h , and h_w is limited to be the accuracy of the derived deflection co-ordinates, which are in turn, dependent on the pixel size and noise of the optical micrographs. Absolute uncertainties of $\Delta s=\Delta L_1=\Delta L_2=\Delta h=\Delta h_w\pm0.1$ μm are defined. We also assume the elastic modulus of a hexagonal ZnO NW [4] is associated with an absolute uncertainty of $\Delta E_{ZnO}=\pm10$ GPa . The absolute uncertainty associated with each calculated energy value can then be computed using the propagation of uncertainty rule for general functions. [19] The absolute uncertainty associated with the energy values determined using the half-arch model, and assuming ideal NW geometry, is given by:

$$\Delta\Gamma_{H-B,reg}=\sqrt{\left(\frac{\partial\Gamma_{H-B,reg}}{\partial E_{ZnO}}\cdot\Delta E_{ZnO}\right)^2+\left(\frac{\partial\Gamma_{H-B,reg}}{\partial s}\cdot\Delta s\right)^2+\left(\frac{\partial\Gamma_{H-B,reg}}{\partial h}\cdot\Delta h\right)^2+\left(\frac{\partial\Gamma_{H-B,reg}}{\partial a_{avg}}\cdot\Delta a_{avg}\right)^2} \tag{S36}$$

The absolute uncertainty associated with the energy values determined using the full-arch model, and assuming ideal NW geometry, is given by:

$$\Delta\Gamma_{F-B,reg}=\sqrt{\left(\frac{\partial\Gamma_{F-B,reg}}{\partial E_{ZnO}}\cdot\Delta E_{ZnO}\right)^2+\left(\frac{\partial\Gamma_{F-B,reg}}{\partial L_1}\cdot\Delta L_1\right)^2+\left(\frac{\partial\Gamma_{F-B,reg}}{\partial L_2}\cdot\Delta L_2\right)^2+\left(\frac{\partial\Gamma_{F-B,reg}}{\partial h_w}\cdot\Delta h_w\right)^2+\left(\frac{\partial\Gamma_{F-B,reg}}{\partial a_{avg}}\cdot\Delta a_{avg}\right)^2} \tag{S37}$$

The absolute uncertainty associated with the energy values determined using the full-arch model, and accounting for the irregular and tapered cross-section of a NW, is given by:

$$\Delta\Gamma_{F-B,irr,taper} = \left(\left(\frac{\partial\Gamma_{F-B,irr,taper}}{\partial E_{ZnO}}\cdot\Delta E_{ZnO}\right)^2 + \left(\frac{\partial\Gamma_{F-B,irr,taper}}{\partial L_1}\cdot\Delta L_1\right)^2 + \left(\frac{\partial\Gamma_{F-B,irr,taper}}{\partial L_2}\cdot\Delta L_2\right)^2 + \left(\frac{\partial\Gamma_{F-B,irr,taper}}{\partial h_w}\cdot\Delta h_w\right)^2 + \right.$$

$$\left. + \left(\frac{\partial\Gamma_{F-B,irr,taper}}{\partial a_1}\cdot\Delta a_1\right)^2 + \left(\frac{\partial\Gamma_{F-B,irr,taper}}{\partial a_2}\cdot\Delta a_2\right)^2 + \left(\frac{\partial\Gamma_{F-B,irr,taper}}{\partial x_{wedge}}\cdot\Delta x_{wedge}\right)^2 + \left(\frac{\partial\Gamma_{F-B,irr,taper}}{\partial\left(da_1/dx\right)}\cdot\Delta\left(da_1/dx\right)\right)^2\right)^{\frac{1}{2}} \quad (S38)$$

The calculated positive and negative bounds of absolute uncertainty for $\Delta\Gamma_{H-B,reg}$, $\Delta\Gamma_{F-B,reg}$, and $\Delta\Gamma_{F-B,irr,taper}$, are provided in Table S9 and S10 (ESI S7).

S7. Nanowire geometry, deflection co-ordinates, deflection model fitting, and interfacial adhesion energy data

Table S4. Geometric parameters for all NW samples.

	$a_{1,wedge}$ (nm)	$a_{2,wedge}$ (nm)	$a_{avg,wedge}$ (nm)	$\frac{da_1}{dx}\left(\frac{nm}{\mu m}\right)$	$Z=\frac{a_1}{a_2}$	$I_{reg,wedge}$ ($m^4 \times 10^{-29}$)	$D_{e,reg,wedge}$ (nm)	$I_{irr,wedge}$ ($m^4 \times 10^{-29}$)	$D_{e,irr,wedge}$ (nm)	L (μm)
NW 1	75.0	59.5	67.2	0.940	1.26	1.11	134.5	1.64	123.6	44.33
NW 2	107.1	85.5	96.3	-0.770	1.25	4.65	192.6	6.83	177.4	71.78
NW 3	170.6	179.2	174.9	-1.100	0.95	50.66	349.8	46.32	355.5	76.39
NW 4	256.0	271.6	263.8	0.379	0.94	262.14	527.6	235.44	537.8	85.85
NW 5	130.9	151.6	141.2	-0.958	0.86	21.53	282.5	16.39	295.7	56.74
NW 6	92.6	119.9	106.3	-0.012	0.77	6.91	212.6	4.22	229.6	82.19
NW 7	254.8	306.9	280.8	1.313	0.83	336.68	561.7	237.41	594.8	88.62
NW 8	111.2	112.3	111.8	0.244	0.99	8.44	223.5	8.30	224.2	62.78
NW 9	94.7	131.4	113.0	0.041	0.72	8.84	226.1	4.69	248.5	63.44
NW 10	268.5	295.1	281.8	-0.063	0.91	341.27	563.6	286.86	580.9	76.26
NW 11	85.0	98.4	91.7	0.000	0.86	3.83	183.4	2.91	192.1	50.53

Table S5. Deflection co-ordinates (Part 1: NW arches 1-6) obtained from interferometric analysis of fringe patterns.

NWA 1		NWA 2		NWA 3		NWA 4		NWA 5		NWA 6	
x (μm)	y (μm)	x (μm)	y (μm)	x (μm)	y (μm)	x (μm)	y (μm)	x (μm)	y (μm)	x (μm)	y (μm)
-13.300	0.000	-27.873	0.000	-23.802	0.000	-18.047	0.000	-13.424	0.000	-14.541	0.000
-11.980	0.101	-25.757	0.101	-22.447	0.101	-15.839	0.101	-12.102	0.101	-13.147	0.101
-11.218	0.203	-24.149	0.203	-20.923	0.203	-14.395	0.203	-10.169	0.203	-12.260	0.203
-10.558	0.304	-22.203	0.304	-19.907	0.304	-12.951	0.304	-8.949	0.304	-11.246	0.304
-10.102	0.405	-21.102	0.405	-18.638	0.405	-11.677	0.405	-7.271	0.405	-10.232	0.405
-9.492	0.506	-20.002	0.506	-17.706	0.506	-10.149	0.506	-5.949	0.506	-9.219	0.506
-8.934	0.608	-18.479	0.608	-16.860	0.608	-8.875	0.608	-4.170	0.608	-8.395	0.608
-8.477	0.709	-17.548	0.709	-16.098	0.709	-7.176	0.709	3.865	0.608	-7.381	0.709
-8.071	0.810	-16.533	0.810	-14.743	0.810	-5.563	0.810	5.695	0.506	-6.304	0.810
-7.563	0.911	-15.348	0.911	-13.897	0.911	-3.694	0.911	7.576	0.405	-5.290	0.911
-7.157	1.013	-14.417	1.013	-13.050	1.013	3.355	0.911	8.949	0.304	-4.340	1.013
-6.650	1.114	-13.571	1.114	-12.119	1.114	4.968	0.810	10.932	0.203	4.467	1.013
-6.244	1.215	-12.894	1.215	-11.188	1.215	7.431	0.709			5.481	0.911
-5.888	1.316	-11.878	1.316	-10.426	1.316	8.535	0.608			6.241	0.810
-5.431	1.418	-10.863	1.418	-9.495	1.418	9.894	0.506			7.128	0.709
-4.975	1.519	-9.932	1.519	-8.479	1.519	10.913	0.405			7.952	0.608
-4.518	1.620	-8.747	1.620	-7.632	1.620	12.442	0.304			8.712	0.506
-4.112	1.721	-7.986	1.721	-6.870	1.721	13.631	0.203			9.409	0.405
-3.604	1.823	-7.055	1.823	-5.770	1.823	15.669	0.101			10.232	0.304
5.431	2.025	-5.447	1.924	-4.839	1.924					11.119	0.203
6.041	1.924	12.325	1.924	-3.738	2.025					12.133	0.101
6.548	1.823	13.256	1.823	10.145	2.228						
7.107	1.721	14.271	1.721	10.992	2.126						
7.564	1.620	15.118	1.620	12.854	2.025						
8.020	1.519	15.964	1.519	14.463	1.924						

8.426	1.418	16.725	1.418	15.563	1.823
8.934	1.316	17.402	1.316	16.918	1.721
9.391	1.215	18.164	1.215	18.018	1.620
9.848	1.114	18.841	1.114	19.034	1.519
10.203	1.013	19.518	1.013	19.965	1.418
10.609	0.911	20.195	0.911	20.897	1.316
11.066	0.810	20.957	0.810	21.828	1.215
11.472	0.709	21.465	0.709	22.590	1.114
11.827	0.608	22.142	0.607	23.775	1.013
12.335	0.506	22.903	0.506	24.537	0.911
12.690	0.405	23.580	0.405	25.384	0.810
13.249	0.304	24.172	0.304	26.145	0.709
13.655	0.203	25.019	0.202	27.161	0.608
14.315	0.101	25.611	0.101	28.008	0.506
14.975	0.000	26.373	0.000	28.854	0.405
		27.219	-0.101	29.616	0.304
				30.717	0.203
				31.563	0.101
				32.918	0.000

Table S6. *Deflection co-ordinates (Part 2: NW arches 7-11) obtained from interferometric analysis of fringe patterns.*

NWA 7		NWA 8		NWA 9		NWA 10		NWA 11	
x (μm)	y (μm)	x (μm)	y (μm)	x (μm)	y (μm)	x (μm)	y (μm)	x (μm)	y (μm)
-29.081	0.000	-9.504	0.000	-11.429	0.000	-19.810	0.000	-5.757	0.000
-27.053	0.101	-8.300	0.101	-9.524	0.101	-14.603	0.203	-5.030	0.101
-25.660	0.203	-7.286	0.203	-8.381	0.203	-10.921	0.405	-4.631	0.203
-23.886	0.304	-6.082	0.304	-7.365	0.304	-5.206	0.608	-3.868	0.304
-22.112	0.405	-5.005	0.405	-6.476	0.405	4.825	0.608	-3.396	0.405
-20.972	0.506	-3.548	0.506	-5.333	0.506	8.762	0.405	-2.524	0.506
-19.388	0.608	-1.837	0.608	-4.444	0.608	12.571	0.203	-1.725	0.608
-17.043	0.709	1.964	0.608	-3.175	0.709	16.889	0.000	2.052	0.608
3.738	0.709	3.485	0.506	3.175	0.709			2.779	0.506
5.322	0.607	5.005	0.405	4.444	0.607			3.650	0.405
7.096	0.506	6.146	0.304	5.587	0.506			4.195	0.304
8.807	0.405	7.413	0.203	6.603	0.405			4.885	0.203
10.201	0.304	8.617	0.101	8.000	0.304			5.321	0.101
12.355	0.202	9.757	0.000	9.016	0.202			6.047	0.000
		11.088	-0.101					6.410	-0.101
		12.545	-0.203					7.173	-0.203
		14.636	-0.304						

Table S7. *Deflection curve fitting parameters, h_w , s , and coefficient of regression, r^2 , for all NW arches using the 'half-arch' model*

	Left side			Right side		
	h_w (μm)	s (μm)	r^2	h_w (μm)	s (μm)	r^2
NWA 1	2.56	16.32	0.9866	2.49	15.32	0.9980
NWA 2	2.53	35.62	0.9880	2.84	27.98	0.9977
NWA 3	2.90	38.15	0.9970	3.03	39.37	0.9921
NWA 4	1.10	22.34	0.9971	0.89	16.50	0.9906
NWA 5	1.29	28.53	0.9981	0.57	13.56	0.9975
NWA 6	1.66	23.42	0.9990	1.23	14.00	0.9986
NWA 7	0.89	19.67	0.9960	0.82	19.48	0.9977
NWA8	0.96	15.72	0.9927	1.05	18.42	0.9955
NWA 9	0.82	11.58	0.9899	1.80	30.84	0.9986
NWA 10	0.62	16.72	0.9939	1.06	29.53	0.9993
NWA 11	1.02	8.92	0.9915	1.23	10.30	0.9938

Table S8. *Deflection curve fitting parameters, h_w, L_1, L_2, x_{wedge} and coefficient of regression, r^2, for all NW arches using the 'full-arch' model, when considering non-tapered and tapered geometry.*

	Non-tapered					Tapered					
	h_w (μm)	L_1 (μm)	L_2 (μm)	r^2_L	r^2_R	h_w (μm)	L_1 (μm)	L_2 (μm)	x_{wedge} (μm)	r^2_L	r^2_R
NWA 1	2.53	17.26	15.12	0.9989	0.9987	2.21	19.42	12.24	14.33	0.9980	0.9981
NWA 2	2.16	46.03	18.64	0.9961	0.9975	2.72	39.81	28.46	36.82	0.9980	0.9991
NWA 3	2.80	37.69	36.96	0.9980	0.9985	2.21	26.74	42.04	30.71	0.9994	0.9996
NWA 4	1.08	22.29	20.91	0.9996	0.9962	1.07	22.62	20.43	21.79	0.9996	0.9962
NWA 5	0.78	15.46	20.14	0.9977	0.9970	0.72	13.73	21.37	17.34	0.9976	0.9954
NWA 6	1.33	20.39	14.22	0.9994	0.9997	1.33	20.37	14.25	18.35	0.9994	0.9996
NWA 7	1.32	30.51	33.36	0.9972	0.9973	1.26	32.22	29.66	36.66	0.9973	0.9980
NWA8	0.95	14.73	16.53	0.9994	0.9994	0.96	15.02	16.35	15.24	0.9993	0.9995
NWA 9	0.83	11.19	14.86	0.9995	0.9980	0.83	11.24	14.81	12.38	0.9995	0.9980
NWA 10	0.78	27.00	19.54	0.9974	0.9994	0.78	26.94	19.65	25.22	0.9974	0.9994
NWA 11	1.28	11.15	10.71	0.9965	0.9978	1.28	11.15	10.71	10.86	0.9965	0.9978

Table S9. *Interfacial adhesion per unit area for all NW arches using the half-arch model (left and right sides) when assuming ideal NW geometry, and the associated negative and positive bounds of absolute uncertainty.*

	Half-arch model					
	$\Gamma_{H-B,reg}$ - left $\left(\text{mJ m}^{-2}\right)$			$\Gamma_{H-B,reg}$ - right $\left(\text{mJ m}^{-2}\right)$		
	nominal	-ve bound	+ve bound	nominal	-ve bound	+ve bound
NWA 1	38.40	25.48	56.45	46.74	30.90	68.97
NWA 2	4.84	3.49	6.59	16.00	11.62	21.70
NWA 3	28.90	22.69	36.44	27.82	21.92	34.98
NWA 4	121.03	86.11	166.28	266.40	179.50	383.05
NWA 5	9.62	6.73	13.48	36.95	20.33	62.54
NWA 6	14.98	10.45	21.07	64.81	42.74	95.86
NWA 7	158.38	107.46	226.15	141.41	94.01	205.22
NWA 8	28.86	18.29	44.09	18.32	11.89	27.43
NWA 9	73.36	44.27	116.71	7.05	5.03	9.71
NWA 10	151.54	91.78	236.09	44.90	31.96	61.58
NWA 11	172.53	105.35	273.42	140.54	89.52	214.77

Table S10. Interfacial adhesion per unit area for all NW arches using the full-arch model when considering ideal as well as irregular and tapered geometry, and the associated negative and positive bounds of absolute uncertainty.

	Full-arch model					
	$\Gamma_{F-B,reg}$ $\left(\text{mJ m}^{-2}\right)$			$\Gamma_{F-B,irr,taper}$ $\left(\text{mJ m}^{-2}\right)$		
	nominal	-ve bound	+ve bound	nominal	-ve bound	+ve bound
NWA 1	39.55	26.21	58.22	41.48	21.82	70.65
NWA 2	13.48	9.52	18.76	20.29	13.35	30.44
NWA 3	29.40	23.02	37.17	81.90	56.52	117.34
NWA 4	134.72	95.46	185.74	112.66	76.06	161.76
NWA 5	25.39	15.71	39.35	41.30	22.57	72.16
NWA 6	37.73	25.28	55.02	26.54	16.50	41.47
NWA 7	51.32	38.11	67.93	17.04	10.59	26.26
NWA 8	29.23	18.46	44.78	25.09	14.52	41.06
NWA 9	52.54	31.94	83.05	32.43	17.88	55.67
NWA 10	71.75	47.09	105.11	64.02	40.88	96.62
NWA 11	121.29	78.01	183.75	99.58	59.85	160.25

References

1. T. H. G. Megson, *Structural and Stress Analysis*, Butterworth-Heinemann, Oxford, UK, 2nd edn., 2005.
2. G. Stan, C. V. Ciobanu, P. M. Parthangal and R. F. Cook, *Nano Lett.*, 2007, **7**, 3691-3697.
3. R. Agrawal, B. Peng, E. E. Gdoutos and H. D. Espinosa, *Nano Lett.*, 2008, **8**, 3668-3674.
4. A. Roy, J. L. Mead, S. Wang and H. Huang, *Scientific Reports*, 2017, **7**, 9547.
5. M. Vable, *Intermediate mechanics of materials*, Oxford University Press, New York, NY, USA, 2008.
6. M. P. de Boer and T. A. Michalske, *J. Appl. Phys.*, 1999, **86**, 817-827.
7. K. J. M. Bishop, C. E. Wilmer, S. Soh and B. A. Grzybowski, *Small*, 2009, **5**, 1600-1630.
8. J. N. Israelachvili, *Intermolecular and Surface Forces*, Academic Press, London, UK, 3rd edn., 2011.
9. M. R. Houston, R. T. Howe and R. Maboudian, *J. Appl. Phys.*, 1997, **81**, 3474-3483.
10. F. W. DelRio, M. P. de Boer, J. A. Knapp, E. David Reedy, P. J. Clews and M. L. Dunn, *Nat Mater*, 2005, **4**, 629-634.
11. H. C. Hamaker, *Physica*, 1937, **4**, 1058-1072.
12. I. E. Dzyaloshinskii, E. M. Lifshitz and L. P. Pitaevskii, *Adv. Phys.*, 1961, **10**, 165-209.
13. A. Meurk, P. F. Luckham and L. Bergström, *Langmuir*, 1997, **13**, 3896-3899.
14. T. J. Senden and C. J. Drummond, *Colloids Surf. Physicochem. Eng. Aspects*, 1995, **94**, 29-51.
15. J. Mahanty and B. W. Ninham, *Dispersion Forces*, Academic Press, New York, NY, USA 1976.
16. V. A. Parsegian, *Van der Waals Forces: A Handbook for Biologists, Chemists, Engineers, and Physicists*, Cambridge University Press, 2005.
17. L. Bergström, *Adv. Colloid Interface Sci.*, 1997, **70**, 125-169.
18. D. B. Hough and L. R. White, *Adv. Colloid Interface Sci.*, 1980, **14**, 3-41.
19. C. Ratcliffe and B. Ratcliffe, *Doubt-Free Uncertainty In Measurement: An Introduction for Engineers and Students*, Springer International Publishing, Cham, Switzerland, 2015.